

Hot extremes have become drier in the United States Southwest

Karen A. McKinnon ¹[∞], Andrew Poppick ⁰² and Isla R. Simpson ⁰³

The impacts of summer heat extremes are mediated by humidity. Increases in temperatures due to human-caused climate change are generally expected to increase specific humidity; however, it remains unclear how humidity extremes may change, especially in climatologically dry (low-humidity) regions. Here we show that specific humidity on dry days during summer (defined here as July-September) has decreased over the past seven decades in the United States Southwest, and that the greatest decreases co-occur with the hottest temperatures. Hot, dry summers have anomalously low evapotranspiration that is linked to low summer soil moisture. The recent decrease in summer soil moisture is explained by declines in June soil moisture, whereas the interannual variability is controlled by summer precipitation. Future projections of hot, dry days in the Southwest are uncertain due to the large spread in the Coupled Model Intercomparison Project phase 6 (CMIP6) trends in soil moisture and precipitation through 2100.

he semi-arid climate of the United States Southwest (hereafter Southwest) has climatologically low precipitation, soil moisture and humidity¹. Against this backdrop of semi-arid conditions, increased atmospheric demand for moisture due to increased temperatures and/or decreased humidity can have three major adverse consequences, particularly during the summer: increases in fire risk²-6, increases in evaporative demand from surface reservoirs¹ and increases in tree mortality⁵. While a substantial body of work has focused on the important role of rising temperatures in the Southwest in causing each of these impacts (for example, refs. ⁹⁻¹¹), there has been less focus on changes in specific humidity.

Theory^{12,13} suggests that specific humidity will generally increase with global warming due to the Clausius–Clapeyron relationship and increased evaporation from the ocean, but it is not clear if the prediction from theory holds for dry regions such as the Southwest or across the temperature distribution. Indeed, some weather stations across the Southwest show negative trends in annual-mean dew point from 1980 to 2010¹⁴ and climate models project that the changes in specific humidity on the hottest days, although positive, will be less than those on average temperature days due to land–atmosphere interactions^{15,16}. Together, these results point to the importance of identifying the origin of observed changes in Southwest humidity, including their temperature dependence, to determine whether specific humidity changes will amplify or damp the effects of temperature increases on the atmospheric demand for moisture.

Here, we analyse temperature and specific humidity from in situ measurements, reanalyses and climate models to determine how and why dry extremes on hot summer days have changed over the past seven decades and may change in the future. We focus on changes in the distribution of specific humidity conditional on fixed temperature thresholds, as opposed to joint exceedances of both variables, to identify changes in the temperature-specific humidity relationship rather than changes in hot, dry extremes caused by increases in temperature alone.

Humidity decreases are amplified at hot temperatures

We first estimate changes in specific humidity on dry days during summer. Summer is defined as July-August-September (JAS), the climatologically warmest 3 months in the Southwest (defined by the outline in Fig. 2a). Our approach is demonstrated at two example locations from the Integrated Surface Database (ISD; ref. ¹⁷) in Fig. 1. The middle panels show summer temperature (T') and specific humidity (q') anomalies from 1973 to 2019 at Perry Stokes Airport, Colorado, and Fresno Yosemite International Airport, California. These stations were chosen because they show distinct underlying T' versus q' relationships: q' generally decreases with T' at Perry Stokes, whereas it increases with T' at Fresno, although the relationships are nonlinear with different behaviour at the centre and tails of their distributions. We quantify the dependence of q' on T' using semiparametric quantile smoothing splines for the 5th, 50th and 95th percentile of q' (black lines in middle panels of Fig. 1). While the focus of this work is on low-humidity days, described with the 5th percentile (q_5'), we present the other two percentiles for context.

To assess if the T' versus q'_5 relationship is changing as the planet warms, we allow both the average value of q_5' and the shape of the T'versus q_5' spline to vary linearly with the low-pass filtered (1/10 yr⁻¹ frequency cutoff) global mean temperature anomaly (GMTA) using the methods of ref. 19 (Methods). We choose GMTA rather than time as our covariate since anthropogenic influence is not necessarily linear in time. The method has previously been shown to perform well for synthetic data with properties similar to daily T' and q' (ref. ¹⁹). The fitted model provides an estimate of q'_5 for any co-occurring local T' and GMTA, so can be queried to quantify how q_5' has changed with increasing GMTA. The total estimated change over 1973-2019 at Perry Stokes and Fresno is illustrated by comparing the grey and black lines in Fig. 1c,f. At both locations, there has been a decrease in q'_5 when T' is at the 95th percentile (hereafter, $q'_{5,T'95}$), as shown by the change along the vertical red line in Fig. 1c,f.

We perform the same analysis at all high-quality ISD stations in the United States with near-continuous records from 1973 to 2019 (Methods), with a focus on changes in $q'_{5,T'95}$. Across the Southwest, $q'_{5,T'95}$ has decreased by an average of $1.05\,\mathrm{g\,kg^{-1}}$ per 1°C increase in GMTA or $0.94\,\mathrm{g\,kg^{-1}}$ since 1973 on the basis of the estimated $0.9\,\mathrm{^{\circ}C}$ warming in GMTA over that period (Fig. 2a). The distribution of trends is skewed toward greater decreases, such that

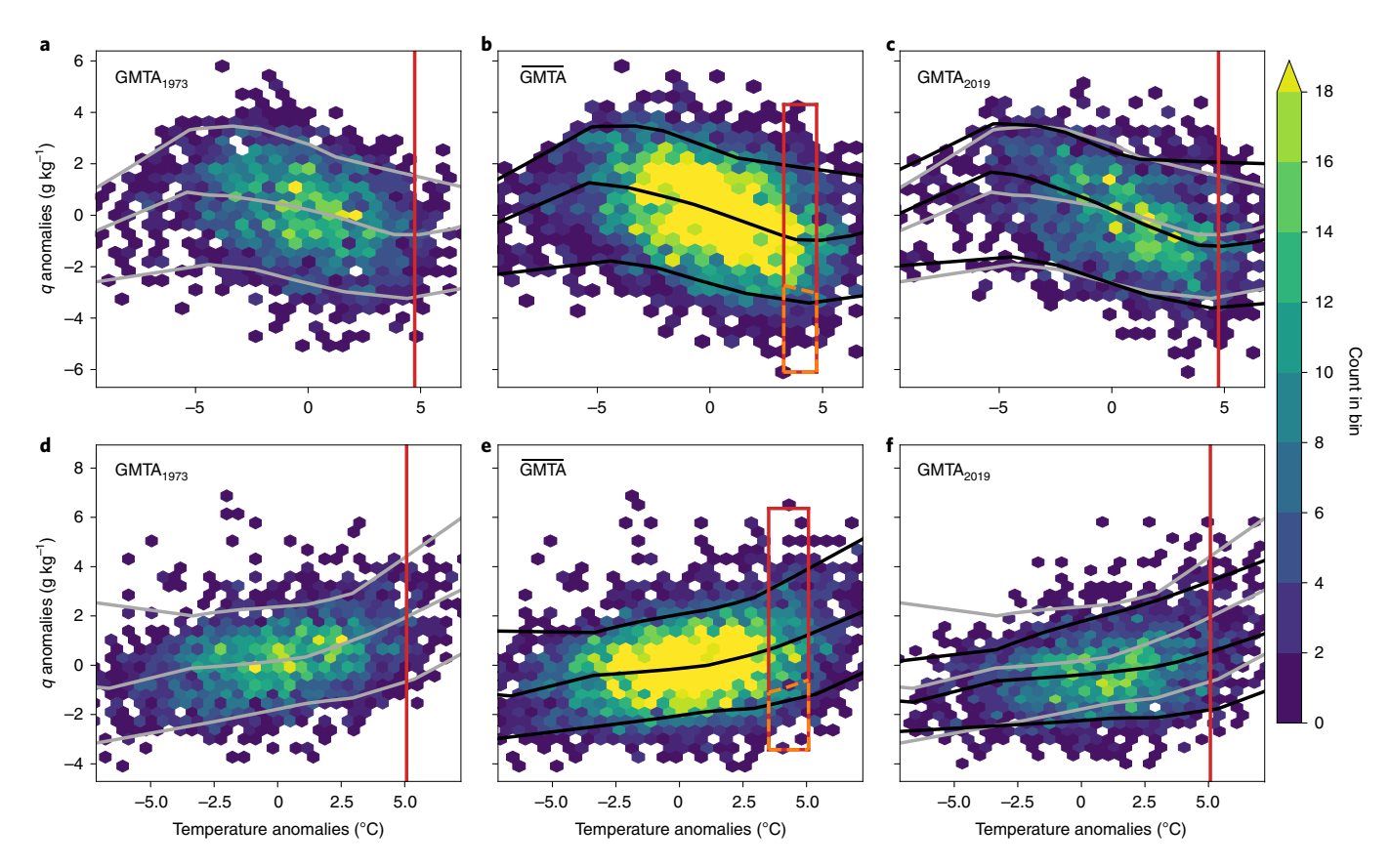


Fig. 1 | Changes in the distribution of specific humidity as a function of increasing global mean temperature anomalies (GMTA) and local temperature. **a**, Observed summer daily-average temperature and specific humidity anomalies at Perry Stokes Airport in southern Colorado for 1973-1995 (two-dimensional histogram shown in colours). The relationship between T' and q' is summarized by the quantile smoothing spline fit conditional on the 1973 low-pass filtered GMTA of -0.43 °C for the 5th, 50th and 95th percentiles of q'. **b**, As in **a**, but for data from the full 1973-2019 period, and with the quantile smoothing spline fit conditional on the average GMTA (0 °C by definition, black lines). **c**, As in **a**, but for data from the second half of the record (1996-2019), and with the quantile smoothing spline fit conditional on the 2019 low-pass filtered GMTA of 0.51 °C (black lines). The spline fits from **a** are reproduced in grey to show changes in the temperature-specific humidity relationship as a function of increasing GMTA. **d**, As in **a**, but for Fresno Yosemite Airport in central California. **e**, As in **b**, but for Fresno Yosemite Airport. **f**, As in **c**, but for Fresno Yosemite Airport. The vertical lines in **a**, **c** (**d**, **f**) show the 95th percentile of temperature anomalies for Perry Stokes Airport (Fresno Yosemite Airport) calculated over the full record. The amplification index can be visualized graphically in **b**, **e** as the count of hot, dry days (dashed orange polygon) normalized by the count of hot days (red polygon).

a quarter of the stations in the Southwest, primarily in California, have decreases in excess of $2\,g\,kg^{-1}$ per 1°C increase in GMTA. To contextualize these changes, the empirical 5th percentile of specific humidity on hot days averaged across ISD stations in the Southwest for 1973-2019 is $4.31\,g\,kg^{-1}$; thus, the average magnitude of the decreases in specific humidity on hot, dry days since 1973 is over 20% of the baseline value.

It is also possible to examine how q_5' has changed conditional on different percentiles of T'. A consistent picture emerges across the region where the magnitude of the decrease in q_5' increases with the co-occurring T' (Fig. 2b). The area-weighted average (Methods) shows that q_5' has increased when T' is low (<26th percentile), exhibits a small decrease of 0.27 gkg⁻¹ per 1°C increase GMTA on days with the median T' and shows increasingly large decreases at higher T', with an average decrease of 1.32 gkg⁻¹ per 1°C increase GMTA when T' is at the 99th percentile. Due to this amplification, analyses of changes in q_5' without accounting for the relationship with T' would underestimate the changes on hot days, when the impacts are greatest.

Hot days have become drier since 1950

The foregoing analysis offers the advantage of using direct measurements from weather stations of the near-surface layer but is

hindered by data availability. Spatially, only 28 high-quality stations are available across the region, which is topographically diverse; further, all stations are at airports, raising concerns that they are not representative of the region as a whole. Temporally, the relatively short duration of the data record (48 yr, 1973–2019) provides only a limited view into the potential role of low-frequency variability versus anthropogenic forcings in contributing to the observed trends.

To address both of these issues, we first turn to additional sources of information. To allow for intercomparison between data sources in terms of both trends and variability, we define an annual amplification index for the full Southwest region. The index is the average probability across the region of having a dry day given the occurrence of a hot day. A hot day is defined at each location as a day in the 85th-95th percentile range of temperature (red polygon in Fig. 1b,e) and a dry day has a specific humidity below the temperature-dependent 10th quantile of specific humidity for a GMTA of zero (dashed orange polygon in Fig. 1b,e). Both thresholds are estimated using the full record and do not change in time. Counts are summed across stations, weighted by the area they represent, to produce the annual amplification index (Methods). By definition, the average amplification index over time is 0.1, meaning 10% of hot days in a summer were also dry. A higher amplification index indicates that a greater fraction of hot days were dry in a

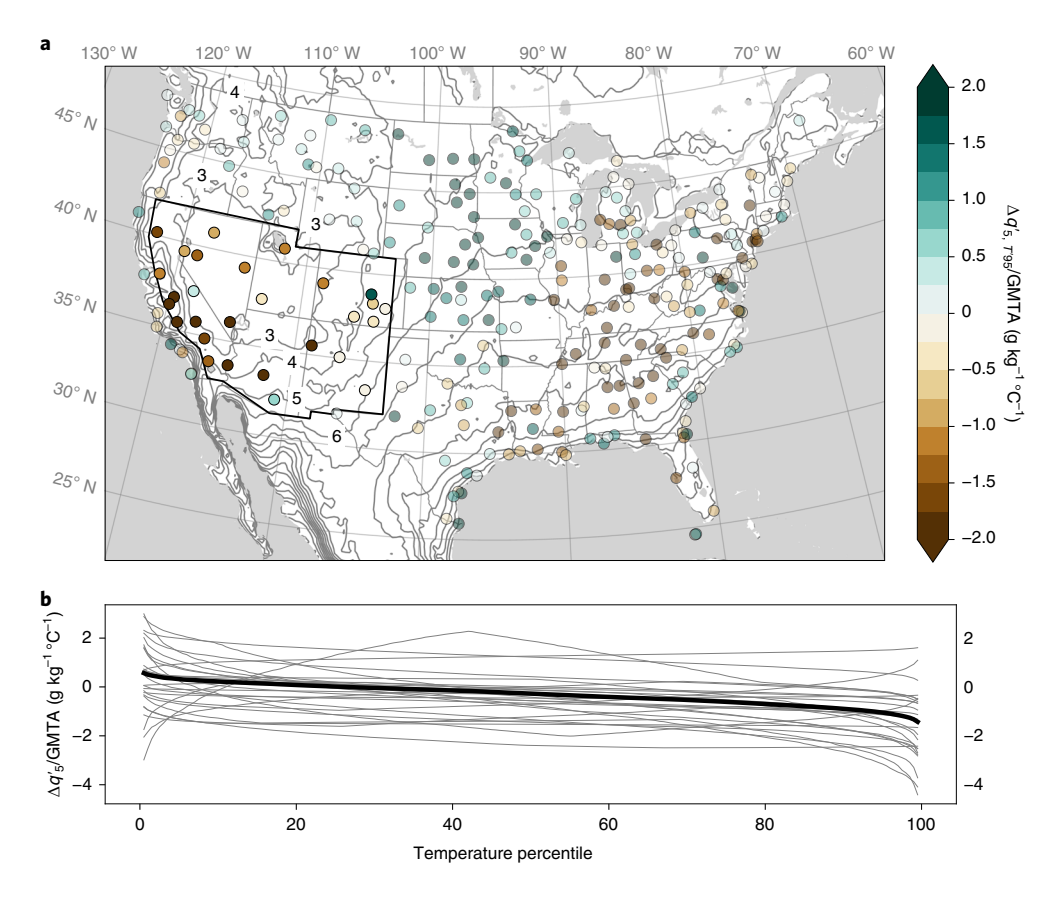


Fig. 2 | Decreases in specific humidity in the American Southwest are amplified on hot days. **a**, Estimated changes in the 5th percentile of specific humidity on hot (95th percentile in temperature anomalies) days $(q'_{5,T'95})$ for a 1°C increase in GMTA at high-quality ISD stations across the continental United States. The Southwest domain is outlined in black. Contours show the 5th percentile of July-August-September specific humidity from ERA5. Contour labels are shown around the Southwest domain; the lowest contour is $3 \, \text{g kg}^{-1}$ and the contour interval is $1 \, \text{g kg}^{-1}$. **b**, The estimated change in the 5th percentile of specific humidity (q'_5) as a function of temperature percentile at each station in the Southwest (thin grey lines) and the area-weighted average across stations (thick black line).

given summer and, by design, does not reflect changes in temperature alone. The thresholds for hot and dry are less extreme than the percentiles used in the prior analysis because calculating the probability of extreme events through empirical counts is noisier than using a semiparametric model.

As expected, the amplification index calculated using the ISD data from 1973 to 2019, ISD₁₉₇₃, shows a positive trend, with the amplification index hovering around 0.07 from 1973 to 2000 and then rapidly increasing post-2000 (Fig. 3a). In addition, there is substantial interannual variability, with 1979, 1987-1989 and 1993-1995 all exhibiting above-average dryness before the year 2000. We next calculate the same index using the ERA5 reanalysis²⁰ to assess if the index is biased by the spatial distribution and limited number of stations. The two indices closely track each other in both their variability and their trend, and are correlated at 0.89 across their shared period of record of 1979-2019, suggesting that the signal of drying is sufficiently large-scale across the Southwest that it can be captured by a small number of station measurements. Finally, we extend the time-series record using the 12 stations in the region that have measurements beginning in 1950 (ISD₁₉₅₀; Methods) and the JRA-55 reanalysis²¹, the only third-generation reanalysis product that begins before 1979 as of this analysis in October 2020. All four estimates of the index paint a similar picture: the ISD₁₉₅₀ index is correlated with the ISD₁₉₇₃ and ERA5 indices at 0.82 and 0.75, and the JRA-55 index is correlated with the ISD₁₉₅₀, ISD₁₉₇₃ and ERA5 indices at 0.75, 0.88 and 0.92, respectively. Although ERA5 agrees well with the other datasets with respect to the amplification

index, we note that it does not show greater decreases in humidity at hotter temperatures across the full Southwest domain (compare Fig. 2b with Extended Data Fig. 1d), which cannot be explained by its different spatial coverage or trend length (Extended Data Fig. 1c–h). The difference is primarily due to the trends in New Mexico, where the ERA5 dataset is an outlier in its suggestion of large increases in humidity on hot days.

Using all four data sources (ERA5, JRA-55, ISD₁₉₅₀ and ISD₁₉₇₃), we calculate a single average amplification index (black line in both panels of Fig. 3) that spans seven decades. Because the number of datasets being averaged increases over time, we expect more variability during the earlier period; however, the subsequent results are qualitatively similar when using the ISD₁₉₅₀ index alone. By extending the time series before the 1970s, we can see that multiple years in the 1950–1965 period exhibited an increased probability of dry extremes on hot days. This phasing and behaviour is consistent with Atlantic multidecadal variability (AMV): the positive phase of the AMV, which occurred from roughly 1926 to 1965 and 1998 to 2014, causes increased subsidence, decreased precipitation and decreased humidity in the Southwest^{22–24}. However, the recent uptick is unprecedented in the record, suggesting there may be an additional role of human influence.

As an initial estimate of the relative roles of these two factors, we fit a multiple linear regression model for the amplification index using the AMV index and GMTA, both of which are low-pass filtered with a frequency cutoff of $1/10\,\mathrm{yr}^{-1}$. The variance explained by each predictor is nearly identical. A regression model that also includes

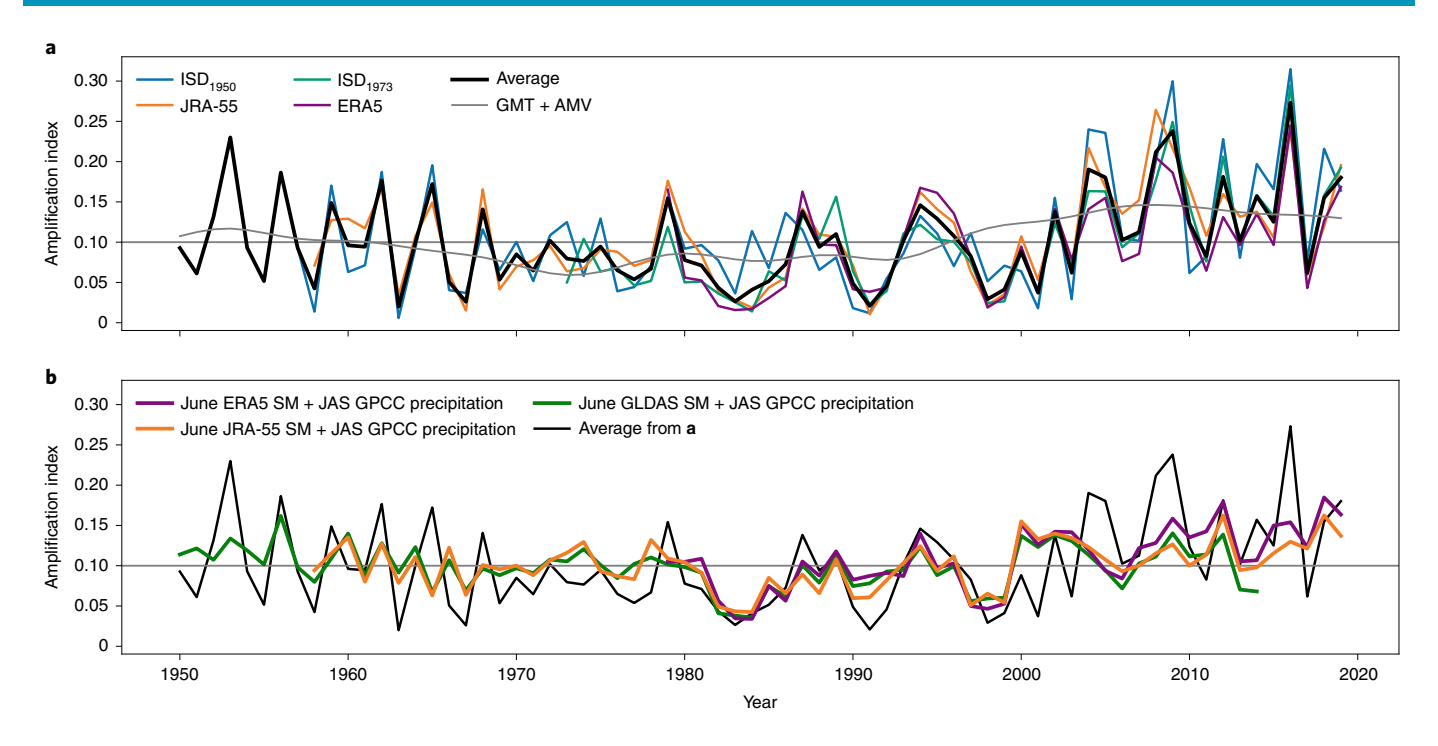


Fig. 3 | The observed and fitted amplification index from 1950 to 2019. a, The amplification index estimated from four datasets (thin coloured lines) and the average across the estimates (thick black line). Note that the number of datasets used to calculate the average changes over time as a function of dataset availability. The low-frequency behaviour (grey line) is estimated on the basis of a regression onto the GMTA and AMV, both which are low-pass filtered with a 1/10 yr⁻¹ cutoff frequency. **b**, The fitted amplification index using June soil moisture (SM) from three different datasets and summer precipitation. The average amplification index (black) is reproduced from **a**. The average amplification index over time is 0.1 by definition.

a December–January–February El Niño/Southern Oscillation (ENSO) index and/or the annual Pacific Decadal Oscillation (PDO) index does not show a statistically significant contribution of either mode (Supplementary Table 1).

Summers with hot, dry extremes have low soil moisture

We next turn to explaining the physical mechanisms that lead to increases in the probability of dry conditions on hot days. From a moisture budget perspective, decreases in near-surface atmospheric humidity can come from three sources: (1) increases in horizontal and/or vertical moisture divergence; (2) decreases in evapotranspiration; and/or (3) increases in precipitation. Due to our focus on the driest days in an already semi-arid region, precipitation is not a relevant factor for directly causing humidity levels well below saturation, leaving us to assess sources (1) and (2).

We first consider the potential role of horizontal moisture divergence. Using ERA5, we calculate the spatial pattern of vertically integrated moisture divergence anomalies (VIMD') associated with low-humidity years as the difference between a composite of the summer VIMD' during the years in the top tercile (33%) of the ERA5-based amplification index, minus those in the bottom tercile. In addition, we compare the time series of the amplification index to that of the summer-averaged, domain-averaged VIMD' (Extended Data Fig. 2b,c). The composite map does not show a coherent pattern of divergence or convergence across the Southwest and neither the raw nor detrended time series are significantly correlated with the raw or detrended amplification index. Since moisture divergence in the Southwest is closely related to the North American monsoon, which varies in its strength throughout the summer season, we additionally compare month-by-month VIMD' to the summer-average amplification index. Unlike August and September, the July composite map shows a coherent region of increased divergence in Arizona, New Mexico and Colorado, and the detrended July VIMD' is weakly but significantly correlated with the detrended amplification

index (Extended Data Fig. 2d-i). This suggests a role of the North American monsoon for the interannual variability in the amplification index that we will return to below.

We next examine whether near-surface drying is associated with a vertical redistribution of moisture from the near-surface to other parts of the atmospheric column through creating top tercile of the ERA5 amplification index minus bottom tercile composites of the average vertical profile of specific humidity between 850 and 200 hPa over the Southwest (note that 47% of the Southwest domain is below 850 hPa on average; for all levels, gridboxes where a given level is below the surface are masked). The vertical profile shows negative specific-humidity anomalies throughout the column (Extended Data Fig. 2a), indicating that the vertical redistribution of moisture, which would result in positive anomalies at another vertical level, cannot explain the near-surface behaviour.

Having found only weak relationships between moisture divergence and the amplification index, we turn to our second physical mechanism, decreases in evapotranspiration. The composite map and time series, made in the same manner as for VIMD', show that years with a high number of dry extremes on hot days are associated with below-average evapotranspiration (the sign of evapotranspiration is defined here as positive from surface to atmosphere) across the Southwest (Fig. 4a). The time series of Southwest-average evapotranspiration and the amplification index are significantly and negatively correlated in their raw and detrended versions (Fig. 4b), suggesting the importance of moisture from the land surface in controlling the probability of dry conditions.

Due to the low soil moisture in the Southwest, evapotranspiration is strongly moisture-limited^{25–27} and closely follows surface soil moisture (Fig. 4c,d). Summer soil moisture is controlled by a simple balance between (1) the initial soil moisture at the beginning of the summer season and (2) changes in moisture availability during summer. Because the contribution of runoff is an order of magnitude smaller than evapotranspiration and precipitation

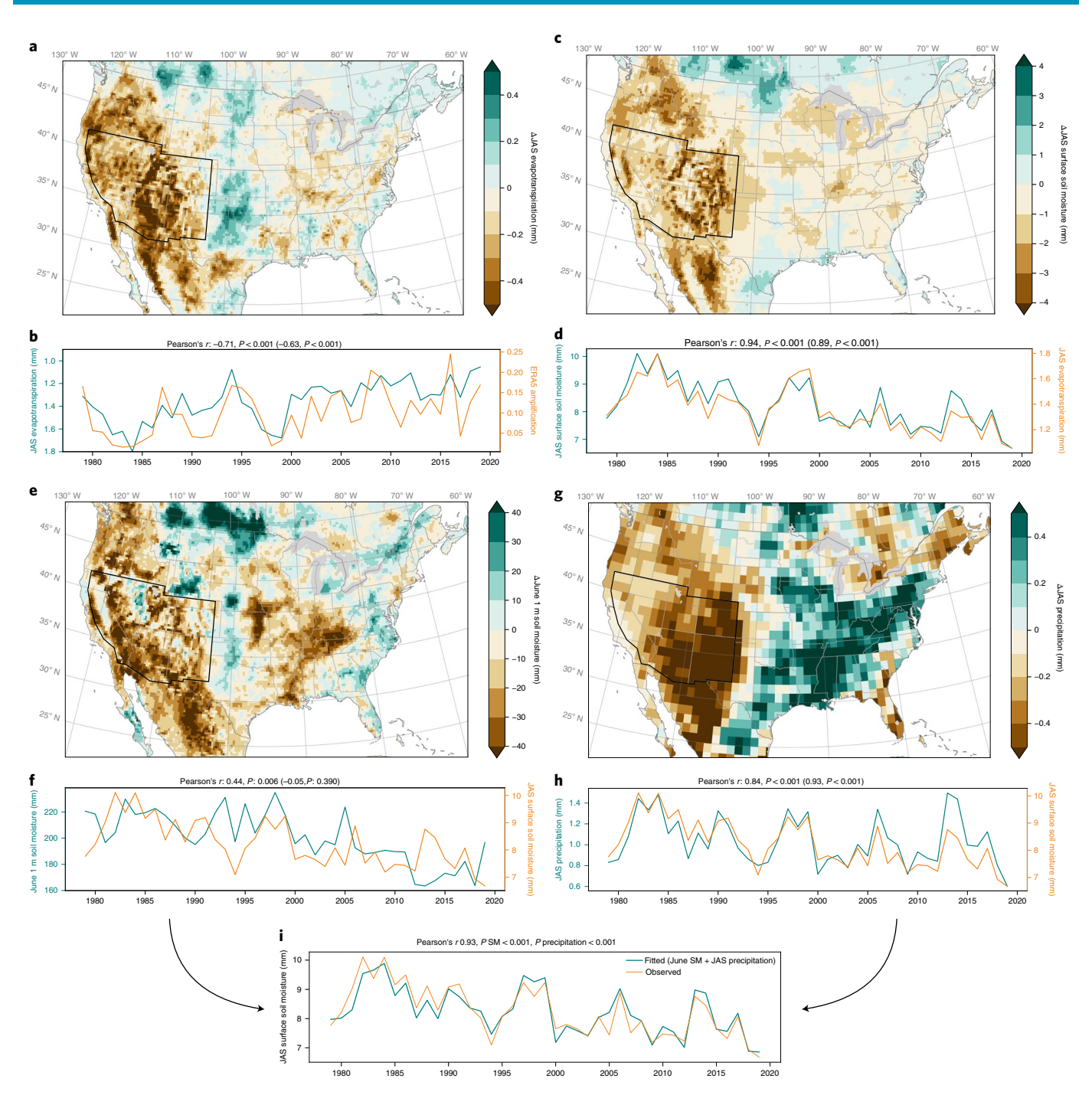


Fig. 4 | Increased probability of hot, dry days linked to reduced evapotranspiration and soil moisture. a, The composite JAS evapotranspiration on years in the top tercile (33%) of the amplification index minus the bottom tercile. b, The time series of the amplification index (orange) and the Southwest-average evapotranspiration (teal, y axis inverted). c, The composite JAS surface soil moisture on years in the bottom tercile of Southwest-average evapotranspiration minus the top tercile. d, The time series of Southwest-average JAS evapotranspiration (orange) and JAS surface soil moisture (teal). e, The composite June 1m soil moisture on years in the bottom tercile of Southwest-average JAS surface soil moisture minus the top tercile. f, The time series of Southwest-average JAS surface soil moisture (orange) and June 1m soil moisture (teal). g, The composite JAS precipitation on years in the bottom tercile of Southwest-average JAS surface soil moisture minus the top tercile. h, The time series of Southwest-average JAS surface soil moisture (orange) and JAS precipitation (teal). i, The observed (orange) and fitted (teal) JAS surface soil moisture; the fitted values are based on a multiple linear regression model using June 1m soil moisture and JAS precipitation as covariates. All data besides precipitation are from ERA5, whereas precipitation is from the Global Precipitation Climatology Centre. Evapotranspiration and precipitation are both the total per day. Raw (detrended) correlation and P values for each time series are shown in the associated title.

(Extended Data Fig. 3) and evapotranspiration is limited by soil moisture, factor (2) is expected to be dominated by precipitation. Using soil moisture from ERA5 and precipitation from the Global Precipitation Climatology Centre (GPCC; ref. ²⁸), we indeed find

that summer soil moisture is very well predicted (Pearson's r=0.93) by June top 1 m soil moisture and JAS precipitation (Fig. 4i). June soil moisture has been decreasing since 1979, consistent with the trend in summer surface soil moisture (Fig. 4e,f). On the other

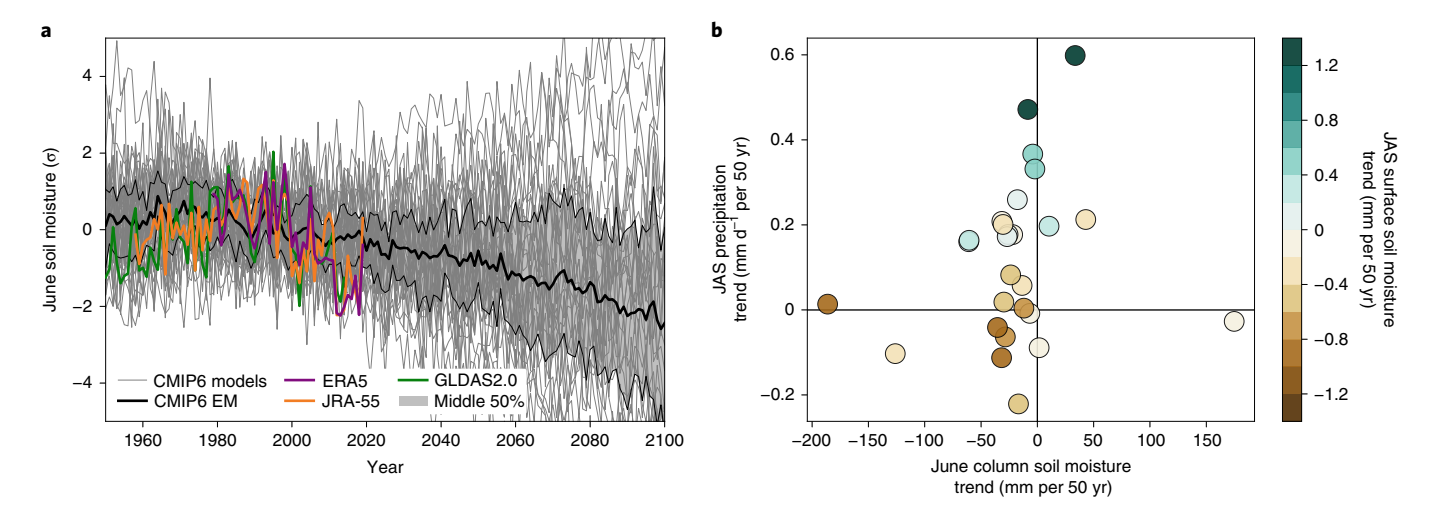


Fig. 5 | CMIP6 projections of June column soil moisture, summer precipitation and summer surface soil moisture. **a**, The June total column soil moisture in the CMIP6 models (grey lines, grey shading outlined in black shows 50% range) and the ensemble mean (black line) from 1950 to 2100 using the historical and SSP5-8.5 scenarios. Three observational estimates of June top 1 m soil moisture are shown in colours. All time series are normalized to have zero mean and unit variance for the overlapping period of 1979–2014. The CMIP6 models show a wide spread of behaviour, although most models project decreases. **b**, The relationship between the linear trend in June column soil moisture (horizontal axis), JAS precipitation (vertical axis) and JAS surface soil moisture (colour) across CMIP6 models. The CMIP6 models are split about trends in JAS surface soil moisture on the basis of the extent to which precipitation increases counterbalance June soil moisture decreases. Trends are calculated over 2015-2100 and normalized to per 50 yr.

hand, summer precipitation does not exhibit a significant trend during the ERA5 period but primarily explains the interannual variability around the trend through its ability to recharge soil moisture levels throughout the summer (Fig. 4g,h).

To link these controls on summer soil moisture back to hot, dry days, we fit a multiple linear regression model for the amplification index using June top 1 m soil moisture from three different sources and summer precipitation from GPCC as predictors; the time series of June soil moisture and summer precipitation are not significantly correlated for any of the soil moisture datasets. The fitted amplification index using soil moisture from either ERA5 (1979-2019), JRA-55 (1958-2019) or NASA Global Land Data Assimilation System v.2.0 (GLDAS2.0 (1950-2014); ref. 29) is correlated with the observed average amplification index at 0.64, 0.51 and 0.50 for their respective periods. The two predictors collectively capture the low-frequency variability and recent uptick in the amplification index, although the fitted amplification index tends to be too high in the 1970s and too low in the recent period (compare the coloured and black lines in Fig. 3b). The regression coefficients for both soil moisture and precipitation are significant in all cases at the 0.01 level (Supplementary Table 1), except for GLDAS2.0 soil moisture, which has a slightly weaker relationship with the amplification index (P = 0.014). The difference emerges because GLDAS2.0 shows a smaller recent decrease in soil moisture than the other two datasets (Fig. 5a), perhaps because it is produced without assimilation of observations of the land state or land-atmosphere coupling.

Future projections are uncertain due to precipitation. We finally consider the implications of our results for future projections. June top 1 m soil moisture has been decreasing since the 1980s (Fig. 5a), which has led to decreased summer soil moisture, decreased evapotranspiration and an increase in the probability of dry conditions on hot days (recall Fig. 4). The observed reduction in June top 1 m soil moisture probably reflects both a forced response and sampling of internal variability^{30,31}, which is substantial in the Southwest due to oceanic teleconnections^{22–24,32,33} and soil moisture memory³⁴. While precipitation plays an important role in the interannual variability of moisture availability, it does not yet appear to have a significant

(Fig. 4h) or forced (for example, ref. ³⁵) trend. How will these factors change in the future? To provide one answer to this question, we use the 28 models with the required data in the CMIP6 archive³⁶ to estimate forced changes from 1950 to 2100 (Methods). The 1950–2014 period uses the historical forcing scenario, whereas the 2015–2100 period uses the energy and resource intensive Shared Socioeconomic Pathways (SSP)5–8.5 scenario³⁷. We note the important caveat that many CMIP6 models have substantial biases in their mean state of soil moisture, precipitation and evapotranspiration in the Southwest (Extended Data Fig. 4), so are likely to exhibit different controls on evapotranspiration than is observed.

Consistent with the behaviour of ERA5 shown in Fig. 4i, summer surface soil moisture in the CMIP6 models is well predicted by June column soil moisture and summer precipitation: the median correlation across the CMIP6 models between the fitted and actual summer soil moisture is 0.95, where the correlation is calculated over the full historical run. The CMIP6 ensemble mean shows a decrease in June soil moisture beginning around 1970 and the majority (82%, 67% significant) of models project a negative trend over 2015–2100 (Fig. 5), reflecting decreased snowpack and increased evapotranspiration during winter and spring^{38,39}. In addition, 70% (48%) of models project a (significant) increase in summer precipitation, which stands in contrast to a current lack of forced precipitation trend. As a result, the models are split about whether summer surface soil moisture will significantly increase (18%), decrease (30%) or not show a significant change (52%) (Fig. 5b). Further, changes in plant physiology driven by increased CO₂ have the potential to alter the historical link between soil moisture and evapotranspiration if plants close their stomata and increase their water use efficiency⁴⁰. Thus, while the trend in summer soil moisture and the probability of hot, dry days appears driven by decreases in pre-summer soil moisture in the historical record, future trends will additionally depend on summer precipitation and the response of the biosphere to elevated CO₂.

In summary, we find that specific humidity has decreased during the summer over the semi-arid Southwest since 1950, with the greatest decreases co-occurring with hot days. In the historical record, the probability of dry conditions on hot days, quantified by the amplification index, exhibits low-frequency variability consistent with the AMV

and a recent uptick that is unprecedented since 1950. The proximal cause of the recent increase in the amplification index is a decrease in evapotranspiration due to low summer soil moisture, which follows from decreases in June soil moisture. The observed decreases in June soil moisture are, on average, simulated by the CMIP6 models; however, the models exhibit substantial biases in their mean state and a large spread in their future projections of soil moisture and rainfall, leaving uncertainties about the future of Southwest dry extremes. Given the recent extreme fire seasons across the Southwest, combined with a growing population and water demand⁴¹, our results highlight the need to quantify the direct impacts of decreasing humidity on the biosphere and water supplies, and to reduce model spread in projections to determine if the recent drying will continue.

Online content

Any methods, additional references, Nature Research reporting summaries, source data, extended data, supplementary information, acknowledgements, peer review information; details of author contributions and competing interests; and statements of data and code availability are available at https://doi.org/10.1038/s41558-021-01076-9.

Received: 4 November 2020; Accepted: 12 May 2021; Published online: 17 June 2021

References

- 1. Seager, R. et al. Whither the 100th meridian? The once and future physical and human geography of America's arid–humid divide. Part I: The story so far. *Earth Interact.* **22**, 1–22 (2018).
- Bradshaw, L. S., Deeming, J. E., Burgan, R. E. & Cohen, J. D. The 1978 National Fire-Danger Rating System: Technical Documentation (USDA Forest Service, 1983).
- 3. Evett, R. R., Mohrle, C. R., Hall, B. L., Brown, T. J. & Stephens, S. L. The effect of monsoonal atmospheric moisture on lightning fire ignitions in southwestern North America. *Agric. For. Meteorol.* **148**, 1478–1487 (2008).
- 4. Fosberg, M. A. Weather in Wildland Fire Management: The Fire Weather Index (USDA Forest Service, 1978).
- Flannigan, M. & Harrington, J. A study of the relation of meteorological variables to monthly provincial area burned by wildfire in Canada (1953–80). J. Appl. Meteorol. 27, 441–452 (1988).
- Williams, A. P. et al. Causes and implications of extreme atmospheric moisture demand during the record-breaking 2011 wildfire season in the southwestern United States. J. Appl. Meteorol. Climatol. 53, 2671–2684 (2014).
- Friedrich, K. et al. Reservoir evaporation in the Western United States: current science, challenges, and future needs. *Bull. Am. Meteorol. Soc.* 99, 167–187 (2018).
- Eamus, D., Boulain, N., Cleverly, J. & Breshears, D. D. Global change-type drought-induced tree mortality: vapor pressure deficit is more important than temperature per se in causing decline in tree health. *Ecol. Evol.* 3, 2711–2729 (2013).
- Allen, C. D. et al. A global overview of drought and heat-induced tree mortality reveals emerging climate change risks for forests. For. Ecol. Manag. 259, 660–684 (2010).
- 10. Williams, A. P. et al. Temperature as a potent driver of regional forest drought stress and tree mortality. *Nat. Clim. Change* **3**, 292–297 (2013).
- Abatzoglou, J. T. & Williams, A. P. Impact of anthropogenic climate change on wildfire across western US forests. *Proc. Natl Acad. Sci. USA* 113, 11770–11775 (2016).
- 12. Byrne, M. P. & O'Gorman, P. A. Understanding decreases in land relative humidity with global warming: conceptual model and GCM simulations. *J. Clim.* **29**, 9045–9061 (2016).
- Chadwick, R., Good, P. & Willett, K. A simple moisture advection model of specific humidity change over land in response to SST warming. *J. Clim.* 29, 7613–7632 (2016).
- Brown, P. J. & DeGaetano, A. T. Trends in US surface humidity, 1930–2010.
 J. Appl. Meteorol. Climatol. 52, 147–163 (2013).

 Coffel, E. D., Horton, R. M., Winter, J. M. & Mankin, J. S. Nonlinear increases in extreme temperatures paradoxically dampen increases in extreme humid-heat. *Environ. Res. Lett.* 14, 084003 (2019).

- Rastogi, D., Lehner, F. & Ashfaq, M. Revisiting recent US heat waves in a warmer and more humid climate. *Geophys. Res. Lett.* 47, e2019GL086736 (2020).
- Smith, A., Lott, N. & Vose, R. The integrated surface database: recent developments and partnerships. *Bull. Am. Meteorol. Soc.* 92, 704–708 (2011).
- Koenker, R., Ng, P. & Portnoy, S. Quantile smoothing splines. Biometrika 81, 673–680 (1994).
- McKinnon, K. A. & Poppick, A. Estimating changes in the observed relationship between humidity and temperature using noncrossing quantile smoothing splines. J. Agric. Biol. Environ. Stat. 25, 292–314 (2020).
- Hersbach, H. et al. The ERA5 global reanalysis. Q. J. R. Meteorol. Soc. 146, 1999–2049 (2020).
- Kobayashi, S. et al. The JRA-55 reanalysis: general specifications and basic characteristics. J. Meteorol. Soc. Jpn II 93, 5-48 (2015).
- Sutton, R. T. & Hodson, D. L. Atlantic Ocean forcing of North American and European summer climate. Science 309, 115–118 (2005).
- Kushnir, Y., Seager, R., Ting, M., Naik, N. & Nakamura, J. Mechanisms of tropical Atlantic SST influence on North American precipitation variability. J. Clim. 23, 5610–5628 (2010).
- Ruprich-Robert, Y. et al. Impacts of the Atlantic multidecadal variability on North American summer climate and heat waves. *J. Clim.* 31, 3679–3700 (2018).
- Teuling, A. et al. A regional perspective on trends in continental evaporation. Geophys. Res. Lett. 36, L02404 (2009).
- Seneviratne, S. I. et al. Investigating soil moisture-climate interactions in a changing climate: a review. Earth-Sci. Rev. 99, 125–161 (2010).
- Vargas Zeppetello, L. R., Battisti, D. S. & Baker, M. B. The origin of soil moisture evaporation 'regimes' J. Clim. 32, 6939–6960 (2019).
- Schneider, U., Fuchs, T., Meyer-Christoffer, A. & Rudolf, B. Global Precipitation Analysis Products of the GPCC (GPCC/DWD, 2008).
- Rodell, M. et al. The global land data assimilation system. Bull. Am. Meteorol. Soc. 85, 381–394 (2004).
- Cayan, D. R. et al. Future dryness in the southwest US and the hydrology of the early 21st century drought. *Proc. Natl Acad. Sci. USA* 107, 21271–21276 (2010).
- Williams, A. P. et al. Large contribution from anthropogenic warming to an emerging North American megadrought. Science 368, 314–318 (2020).
- Ault, T. R. et al. A robust null hypothesis for the potential causes of megadrought in western North America. J. Clim. 31, 3-24 (2018).
- Seager, R., Kushnir, Y., Herweijer, C., Naik, N. & Velez, J. Modeling of tropical forcing of persistent droughts and pluvials over western North America: 1856–2000. J. Clim. 18, 4065–4088 (2005).
- Kumar, S., Newman, M., Wang, Y. & Livneh, B. Potential reemergence of seasonal soil moisture anomalies in North America. *J. Clim.* 32, 2707–2734 (2019).
- Lehner, F., Deser, C., Simpson, I. R. & Terray, L. Attributing the US Southwest's recent shift into drier conditions. *Geophys. Res. Lett.* 45, 6251–6261 (2018).
- Eyring, V. et al. Overview of the Coupled Model Intercomparison Project Phase 6 (CMIP6) experimental design and organization. *Geosci. Model Dev.* 9, 1937–1958 (2016).
- O'Neill, B. C. et al. The Scenario Model Intercomparison Project (ScenarioMIP) for CMIP6. Geosci. Model Dev. 9, 3461–3482 (2016).
- Mankin, J. S., Smerdon, J. E., Cook, B. I., Williams, A. P. & Seager, R. The curious case of projected twenty-first-century drying but greening in the American West. J. Clim. 30, 8689–8710 (2017).
- Cook, B. et al. Twenty-first century drought projections in the CMIP6 forcing scenarios. *Earth's Future* 8, e2019EF001461 (2020).
- Swann, A. L. Plants and drought in a changing climate. Curr. Clim. Change Rep. 4, 192–201 (2018).
- MacDonald, G. M. Water, climate change, and sustainability in the southwest. Proc. Natl Acad. Sci. USA 107, 21256–21262 (2010).

Publisher's note Springer Nature remains neutral with regard to jurisdictional claims in published maps and institutional affiliations.

© The Author(s), under exclusive licence to Springer Nature Limited 2021

Methods

ISD data. Temperature and humidity data are from the ISD (ref. 17) provided by the National Centers for Environmental Information. The database is composed of in situ weather station measurements taken on subdaily timescales and is the only source of publicly available non-remotely sensed humidity data that spans the United States. Humidity information is provided via measurements of dew point. We mark any measurement with a suspect quality control flag as missing. In particular, we remove data points with a source flag of 2, A, B, O or 9; a report type flag of 99999; a call sign flag of 99999; and a quality control flag of V01. We additionally remove days that do not have four or more valid observations. Our ISD-based analysis focuses on two time periods: 1973-2019 and 1950-2019. There is a large increase in the number of weather stations reporting to the ISD database beginning in 1973, so the shorter time period allows for greater selectivity and more complete spatial coverage. In both cases, a given weather station is only included in the analysis if at least 80% of years have less than 20% missing data in both temperature and dew point for the summer season (defined as July-September) of each year and are not entirely missing the first and last 3 yr of the time period of interest. For the 1973-2019 period, we additionally remove stations that have more than one missing year in a row. The station distribution and trends in q_5' for the 1950–2019 period are shown in Extended Data Fig. 5.

Calculating daily-average specific humidity. Daily-average specific humidity $(q \text{ in gkg}^{-1})$ is calculated from subdaily (at least 6-hourly) values of dew point $(T_d \text{ in } {}^{\circ}\text{C})$ and pressure (p in hPa) using the following approximation⁴²:

$$e = 6.112 \exp\left(\frac{17.67T_{\rm d}}{T_{\rm d} + 243.5}\right) \tag{1}$$

$$q = 1,000 \frac{0.622e}{p - 0.378e} \tag{2}$$

Dew point and pressure are converted to specific humidity before performing the daily average.

Anomaly calculation. Daily temperature and specific humidity are considered as anomalies from the climatological seasonal cycle, with the seasonal cycle calculated as the first three seasonal harmonics for temperature and ten harmonics for specific humidity. The larger number of harmonics for specific humidity is necessary in this region because the onset of the North American monsoon in July can lead to a rapid increase in specific humidity over a short period of time. The estimated seasonal cycle for specific humidity using ten harmonics, as well as two alternative methods (low-pass filter and moving average), is shown for two representative ISD stations, one influenced by the North American monsoon and one not, in Extended Data Fig. 6.

ERA5 data. For the calculation of the amplification index using ERA5 (ref. ²⁰), we use 6-hourly 2-m air temperature, 2-m dew point and surface pressure; surface pressure and dew point are used to calculate 6-hourly specific humidity, which is then averaged to calculate the daily-average specific humidity. ERA5 incorporates screen-level observations through optimal interpolation in the land data assimilation system, which is weakly coupled with the full 4D-Var assimilation. To understand the causes of the variability and trend in the amplification index, we use the monthly averaged reanalysis for evapotranspiration, vertically integrated moisture divergence, runoff and soil moisture. The effective accumulation period for evapotranspiration, vertically integrated moisture divergence and runoff is 1 d. We group soil moisture into surface (swvl1, 0-7 cm) and top 1 m (swvl1, swvl2 and swvl3). All ERA5-based analyses span 1979–2019. The trends in q_5' for ERA5 data are shown in Extended Data Fig. 1c,d.

 $\mbox{JRA-55}$ data. For the calculation of the amplification index in JRA-55 (ref. $^{21}),$ we use 6-hourly 2-m air temperature and 2-m specific humidity, which are then averaged to calculate daily-average temperature and specific humidity. We calculate the amplification index using both the analysis and forecast variables; the former incorporates screen-level observations through optimal interpolation but is not subsequently coupled back into the forecast. The results using the analysis output are presented in the main paper. The amplification index calculated using the forecast variables alone, however, is inconsistent with all other estimates of the amplification index in both the low-frequency and high-frequency variability, indicating the importance of the screen-level observations for the reanalysis product. JRA-55 soil moisture is provided as a wetness fraction for three layers of soil; the thickness of the layers depends on the land cover type. We integrate the soil wetness fraction across the top 1 m of soil assuming a vegetation type of broadleaf shrubs with groundcover, which is dominant in the Southwest (for example, Fig. 5 in ref. 43). The layer thicknesses for broadleaf shrubs with groundcover are 0.02 m, 0.47 m and 1 m. All JRA-55-based analyses span 1958-2019. The trends in q_5' for JRA-55 data are shown in Extended Data Fig. 1a,b.

GLDAS data. The GLDAS-based regression model in Fig. 3b uses the top 1 m soil moisture for the 1950–2014 period on the basis of the Noah land surface

model, where the end date is limited by the availability of GLDAS2.0. GLDAS2.0 is forced by the Princeton meteorological forcing dataset*4 and does not use data assimilation (that is, is open loop).

CMIP6 data. We use the following 28 models from the CMIP6 archive, on the basis of their having at least one ensemble member with monthly average total column soil moisture (mrso), surface soil moisture (mrsos) and precipitation (pr) for both the historical and SSP5-8.5 scenarios: ACCESS-CM2, ACCESS-ESM1-5, BCC-CSM2-MR, CAMS-CSM1-0, CESM2, CESM2-WACCM, CMCC-CM2-SR5, CNRM-CM6-1, CNRM-CM6-1-HR, CNRM-ESM2-1, CanESM5, CanESM5-CanOE, EC-Earth3, EC-Earth3-Veg, FGOALS-f3-L, FGOALS-g3, GFDL-CM4, GFDL-ESM4, GISS-E2-1-G, IPSL-CM6A-LR, MIROC-ES2L, MIROC6, MPI-ESM1-2-HR, MPI-ESM1-2-LR, MRI-ESM2-0, NorESM2-LM, NorESM2-MM and UKESM1-0-LL. For CMIP6 models that have more than one ensemble member, we first average the available ensemble members before calculating the ensemble mean such that each model contributes equally to our analysis. The standardized soil moisture anomalies in Fig. 5a are calculated using the 1979-2014 period as a reference, to match the overlapping availability of the three observation-based datasets. The trends in Fig. 5b are calculated over the SSP5-8.5 scenario only, 2015-2100.

Global mean temperature and sea surface temperature modes. GMTA are from the Berkeley Earth Surface Temperature dataset⁴⁵. The time series of the AMV index, the ENSO and the PDO are calculated using monthly average data from ERSSTv.5 (ref. ⁴⁶). The AMV index is calculated using the Climate Variability Diagnostics Package⁴⁷ as per ref. ⁴⁸ by removing the near-global mean (60°S–60°N) sea surface temperature (SST) anomaly from the SST anomaly over the North Atlantic (0°–60°N, 80°W–0°) at each timestep. All analyses with GMTA and AMV use a low-pass filtered time series calculated with a third-order Butterworth filter with a cutoff frequency of 1/10 yr⁻¹. The ENSO index is the 3-month running mean of SST anomalies in the Niño 3.4 region (5°S–5°N, 170°–120°W). The PDO index is created by first regressing the SST anomalies against the Mantua PDO index⁴⁹ for their overlap period to compute a PDO regression map for the North Pacific (20°–70°N), which is then projected onto the SST anomalies to compute the index. Both the ENSO and PDO indices are provided by the National Center for Environmental Information and neither are further low-pass filtered.

Amplification index. The amplification index is the empirical count of hot, dry days normalized by hot days in a given summer. The main analysis shows the index calculated by defining a hot day as one that falls in the 85th–95th percentile range and a dry day as one that falls below the 10th percentile of specific humidity. The amplification index is similar although more noisy (Extended Data Fig. 7) if we instead define a hot day as around the 95th percentile (\pm 5%) and a dry day as below the 5th percentile to match the quantile regression analysis. Because some gridboxes and stations may not have any hot days in a given summer, we first sum the counts across stations or gridboxes, weighted by the area they represent, before performing the division ('Spatial domain and area weighting' below).

Quantile smoothing splines method. To assess changes in the distribution of specific humidity anomalies conditional on the co-occurring local temperature anomalies and GMTA, we use quantile smoothing splines that can vary linearly with GMTA. Specifically, we model a given quantile, τ , of specific humidity anomalies on day t as

$$q_{\tau}'(t) = \beta_{0,\tau} + s_{0,\tau}(T'(t)) + \beta_{1,\tau}G'(t) + G'(t)s_{1,\tau}(T'(t))$$
(3)

where T'(t) is the co-occurring temperature and G'(t) is the low-pass filtered GMTA. Both $s_{0,r}$ and $s_{1,r}$ are functions of T'(t). The first two terms on the right-hand side summarize the quantiles of specific humidity anomalies, including the dependence on local temperature anomalies, for a GMTA of zero. The third term allows changes in specific humidity that are linearly dependent on GMTA to be incorporated, while the fourth term allows the relationship between specific humidity and local temperature to evolve with GMTA. For example, if global warming were associated with a mean increase in specific humidity at quantile τ , as well as a greater increase in specific humidity on days at the 95th percentile of temperature anomalies, this would appear in the model as positive $\beta_{1,\tau}$ and $s_{1,\tau}(T'_{95})$ values, respectively. The terms $s_{0,\tau}(T'(t))$ and $s_{1,\tau}(T'(t))$ are quantile smoothing splines that summarize the potentially nonlinear relationship between a given quantile of specific humidity and temperature anomalies. The complexity of the spline, as measured by the number of change-points, is controlled by a regularization parameter, which was selected in ref. 19 through minimization of a high-dimensional Bayesian Information Criterion⁵⁰. Here, we draw from the results of ref. 19 and model the log of the regularization parameter as linearly related to the standard deviation of the temperature anomalies at each station (see Fig. S5 in ref. 19). We fit the 5th, 10th, 50th, 90th and 95th percentile of specific humidity anomalies, although the focus of the work is primarily on the 5th percentile. A non-crossing constraint is enforced during the fitting procedure following ref. 5 such that a lower percentile of specific humidity anomalies cannot be larger than a higher percentile at any time.

Spatial domain and area weighting. We focus on the American Southwest, defined here as including Colorado, New Mexico, Utah, Arizona, Nevada and non-coastal California (outline in Fig. 2a). We exclude the stations along the California coast from our analysis because their climate is strongly and directly influenced by the neighbouring ocean. Values presented as averages over the domain are weighted by approximations of the amount of area represented by each weather station or gridbox. For the 1973–2019 period, during which stations are more plentiful, the station weights are the areas associated with each station after performing a Voronoi tessellation on all stations in the United States. For the 1950–2019 period, due to the reduced number of stations that border the Southwest domain, the station weights are instead calculated as the minimum distance between a station and any other station within the Southwest domain. Results are insensitive to reasonable choices of station weighting. For the reanalyses, gridboxes are weighted by the cosine of latitude.

Correlations and significance. All correlation values are Pearson correlation coefficients. The effective degrees of freedom used for the estimation of P values is calculated as $n_{\rm eff} = \frac{1-\phi^2}{1+\phi^2} N - k$ (ref. 52). For the raw correlations, k=2, where the reduction of two degrees of freedom is due to controlling for the mean and variance. For the detrended correlations, k=3 due to controlling for a linear time trend. For the regression models, k is equal to the number of predictors (including an intercept term). The value of ϕ is the empirical lag-1 autocorrelation coefficient of the residuals from the regression model. The effective regression model is $y=\beta_0+\beta_1x+\varepsilon$ for the raw correlations and $y=\beta_0+\beta_1x+\beta_2t+\varepsilon$ for detrended correlations. All P values, except those predicting the amplification index with GMTA and AMV, are one-sided, because the expected direction of the relationships is a priori known. Throughout the paper, significance is assessed at the 0.01 level.

Data availability

Data from ISD are publicly available at https://www.ncdc.noaa.gov/isd/data-access. Data from ERA5 are publicly available at https://cds.climate.copernicus.eu. Data from JRA-55 are publicly available at https://cda.ucar.edu/datasets/ds628.1/ (monthly) and https://rda.ucar.edu/datasets/ds628.0/ (daily). Data from GPCC are publicly available at https://psl.noaa.gov/data/gridded/data.gpcc.html. Data from GLDAS2.0 are publicly available at https://ldas.gsfc.nasa.gov/data. Model output from CMIP6 is publicly available at https://ldas.gsfc.nasa.gov/data. Model output from CMIP6 is publicly available at https://esgf-node.llnl.gov/projects/cmip6/. Berkeley Earth global mean temperature is publicly available at http://berkeleyearth.lbl.gov/auto/Global/Land_and_Ocean_complete.txt. ERSSTv.5 data are publicly available at http://berkeleyearth.lbl.gov/auto/Global/Land_and_Ocean_complete.txt. The AMV index was calculated using the Climate Variability and Diagnostics Package, which is publicly available at https://www.cesm.ucar.edu/working_groups/CVC/cvdp/. The PDO index is publicly available at https://www.ncdc.noaa.gov/teleconnections/pdo/. The Niño 3.4 index is publicly available at https://www.cpc.ncep.noaa.gov/data/indices/oni.ascii.txt.

Code availability

Code to fit the non-crossing quantile smoothing splines model is available at https://github.com/karenamckinnon/humidity_variability. Code to perform the analysis and reproduce the figures in the paper is available at https://github.com/karenamckinnon/compound_extremes.

References

- Bolton, D. The computation of equivalent potential temperature. Mon. Weather Rev. 108, 1046–1053 (1980).
- 43. Zheng, W. et al. Improvement of daytime land surface skin temperature over arid regions in the NCEP GFS model and its impact on satellite data assimilation. *J. Geophys. Res.* 117, D06117 (2012).

- Sheffield, J., Goteti, G. & Wood, E. F. Development of a 50-year high-resolution global dataset of meteorological forcings for land surface modeling. J. Clim. 19, 3088–3111 (2006).
- Rohde, R. et al. Berkeley Earth temperature averaging process. Geoinfor. Geostat. 1, 20–100 (2013).
- Huang, B. et al. Extended reconstructed sea surface temperature, version 5 (ERSSTv5): upgrades, validations, and intercomparisons. *J. Clim.* 30, 8179–8205 (2017).
- Phillips, A. S., Deser, C. & Fasullo, J. Evaluating modes of variability in climate models. Eos Trans. Am. Geophys. Union 95, 453–455 (2014).
- 48. Trenberth, K. E. & Shea, D. J. Atlantic hurricanes and natural variability in 2005. *Geophys. Res. Lett.* **33**, L12704 (2006).
- Mantua, N. J., Hare, S. R., Zhang, Y., Wallace, J. M. & Francis, R. C. A Pacific interdecadal climate oscillation with impacts on salmon production. *Bull. Am. Meteorol. Soc.* 78, 1069–1080 (1997).
- Lee, E. R., Noh, H. & Park, B. U. Model selection via Bayesian information criterion for quantile regression models. J. Am. Stat. Assoc. 109, 216–229 (2014).
- Liu, Y. & Wu, Y. Stepwise multiple quantile regression estimation using non-crossing constraints. Stat. Its Interface 2, 299–310 (2009).
- Bretherton, C. S., Widmann, M., Dymnikov, V. P., Wallace, J. M. & Bladé, I. The effective number of spatial degrees of freedom of a time-varying field. *J. Clim.* 12, 1990–2009 (1999).

Acknowledgements

K.A.M. acknowledges support from the National Science Foundation (award no. 1939988). I.R.S. was supported by the National Center for Atmospheric Research (NCAR), which is a major facility sponsored by the National Science Foundation under the Cooperative Agreement 1852977. JRA-55 data were provided by the Research Data Archive of the Computational and Information Systems Laboratory (CISL) at NCAR. Analysis was performed on the Casper cluster supported by by NCAR's CISL. We acknowledge the World Climate Research Programme's Working Group on Coupled Modelling, which is responsible for CMIP, and we thank the climate modelling groups (listed in Methods) for producing and making available their model output. For CMIP, the US Department of Energy's Program for Climate Model Diagnosis and Intercomparison provides coordinating support and led development of software infrastructure in partnership with the Global Organization for Earth System Science Portals.

Author contributions

K.A.M. conceived the study, performed the analysis and wrote the manuscript. A.P. contributed to the development of the method and provided commentary on the manuscript. I.R.S. provided feedback on the analysis and manuscript. Correspondence should be addressed to K.A.M.

Competing interests

The authors declare no competing interests.

Additional information

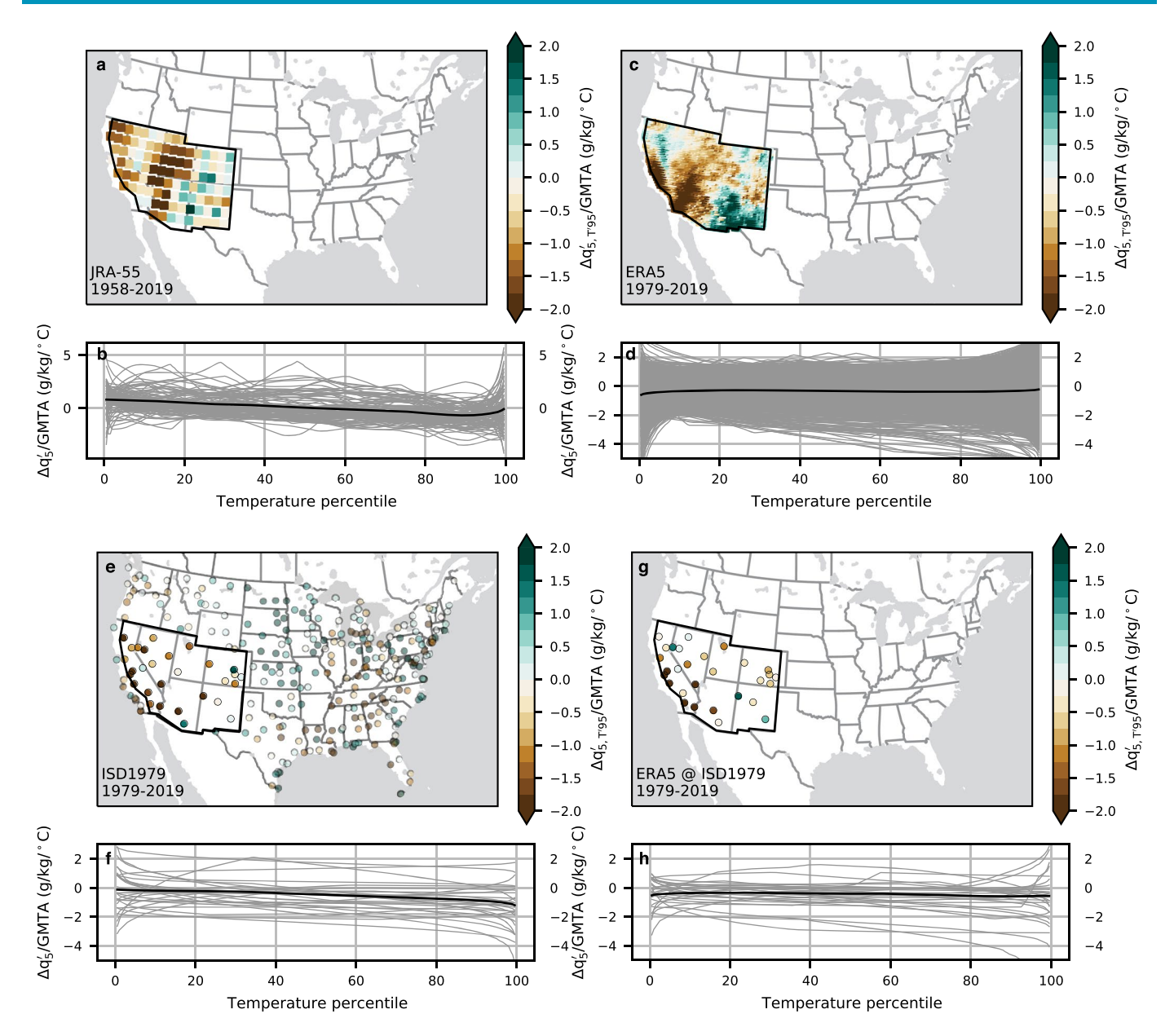
Extended data is available for this paper at https://doi.org/10.1038/s41558-021-01076-9.

Supplementary information The online version contains supplementary material available at https://doi.org/10.1038/s41558-021-01076-9.

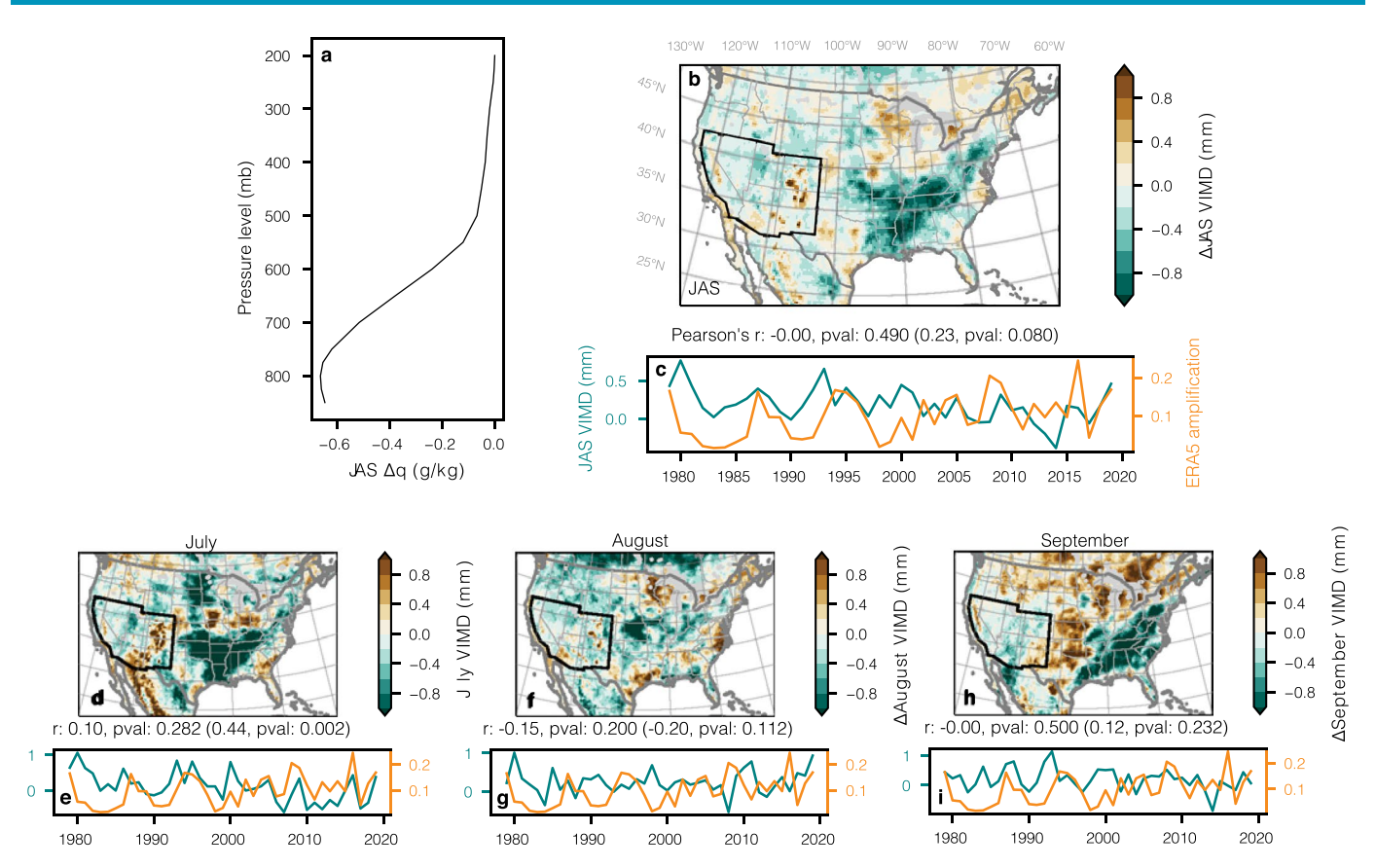
Correspondence and requests for materials should be addressed to K.A.M.

Peer review information *Nature Climate Change* thanks Tim Cowan, Clemens Schwingshackl and the other, anonymous, reviewer(s) for their contribution to the peer review of this work.

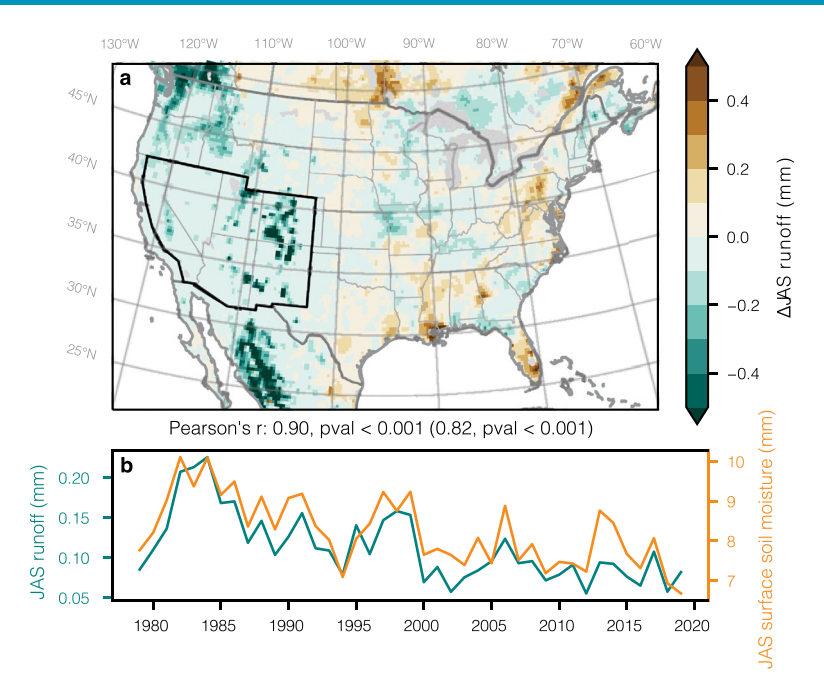
Reprints and permissions information is available at www.nature.com/reprints.



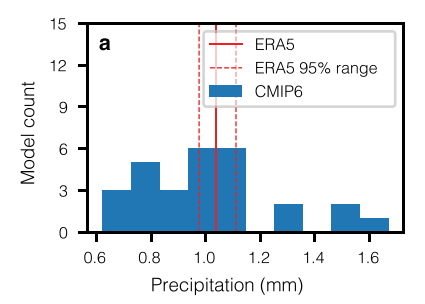
Extended Data Fig. 1 Changes in hot, dry days for JRA-55, ERA5, ISD1979, and ERA5 at locations of Integrated Surface Database stations. As in Fig. 2, but with data from (a, b) JRA-55, (c, d) ERA5, (e, f) Integrated Surface Database (ISD) stations from 1979-2019, and (g, h) ERA5 subset to the locations of the ISD stations in (e). Trends are calculated over the 1958-2019 period for JRA-55, and over the 1979-2019 period for all other maps. The ERA5-based trends in panel (d) uniquely do not show the amplification of drying at hot temperatures. To test whether the difference is due to the different starting point of the ERA5 trends, we recalculate trends in the ISD stations for the 1979-2019 period (panels e and f), which still show the amplification. To test whether the difference is due to the specific locations of the ISD stations, we subset the ERA5 trends to the locations of the ISD stations (panels g and h); this subset does not show the amplification behaviour. In the line plots (panels b, d, f, h), thin grey lines show the trends at each gridbox, and the thick black line is the area-weighted average across gridboxes. Note the different y-scales across the line plots.

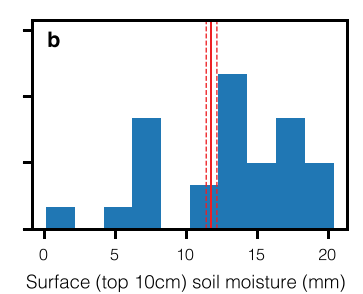


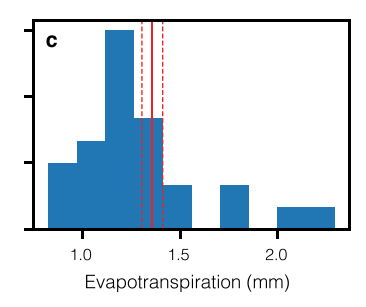
Extended Data Fig. 2 | Vertical and horizontal divergence do not explain the amplification index. a, The composite vertical profile of July–August-September specific humidity from ERA5 on years in the top tercile (33%) of the amplification index minus the bottom tercile. **b**, The composite July–August-September vertically integrated moisture divergence from ERA5 on years in the top tercile of the amplification index minus the bottom tercile. **c**, The time series of the amplification index (orange) and the Southwest-average vertically integrated moisture divergence (teal). (**d-i**) As in (**b**)-(**c**), but for July, August, and September vertically integrated moisture divergence is the total per day.



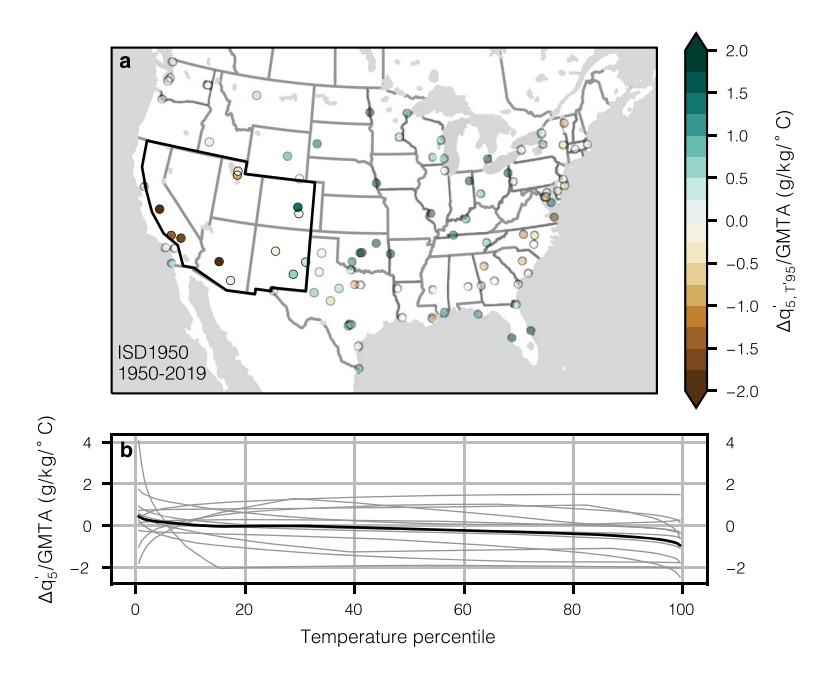
Extended Data Fig. 3 | Runoff covaries with surface soil moisture, but its contribution to the water balance is small. As in Fig. 4, but for runoff from ERA5. Runoff is the total per day.



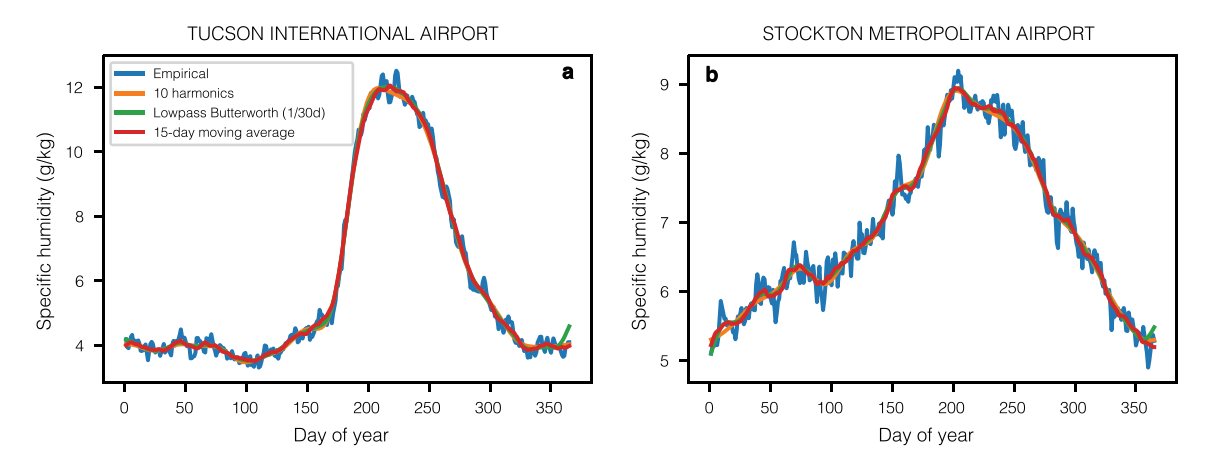




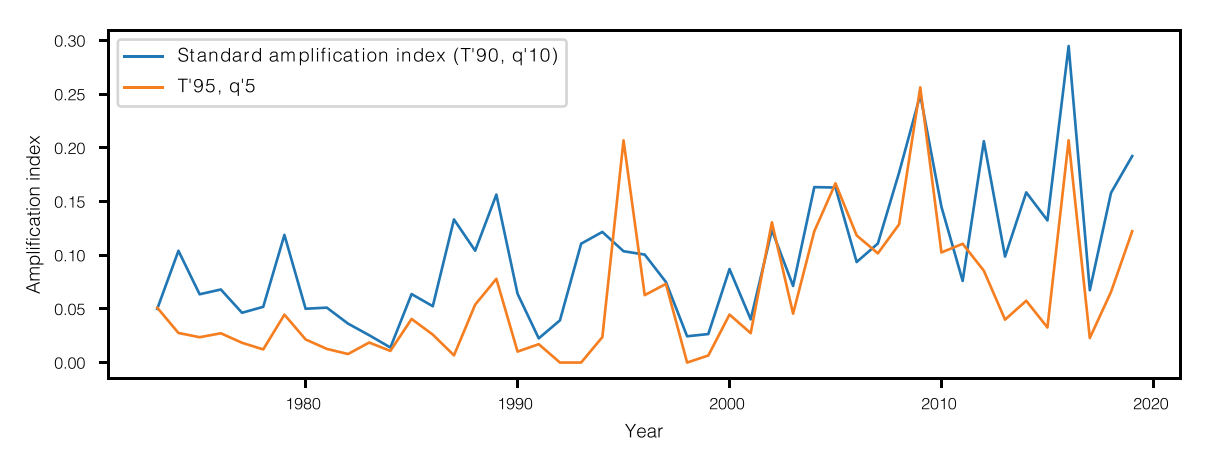
Extended Data Fig. 4 | The CMIP6 models can have large biases in their mean state of precipitation, soil moisture, and evapotranspiration in the Southwest. The distribution of July-August-September (a) average precipitation, (b) surface soil moisture, and (c) evapotranspiration from the 28 CMIP6 models used for Fig. 5 (blue histograms) and ERA5 (red vertical line). The CMIP6 estimates are based on 1979-2014, and the ERA5 estimates are based on 1979-2019; the end date in CMIP6 is the end of the historical scenario simulations. The 95% range shown for ERA5 is calculated by performing a bootstrap of the seasonal mean values with replacement, and provides an estimate of the uncertainty of the mean value due to sampling of internal variability. Surface soil moisture in the CMIP6 models is calculated over the top 10cm, whereas the top soil layer in ERA5 is 7cm; as such, the ERA5 surface soil moisture is multiplied by 10/7 for this comparison.



Extended Data Fig. 5 | Changes in hot, dry extremes in Integrated Surface Database stations from 1950-2019. As in Fig. 2, but with the limited number of Integrated Surface Database stations with data beginning in 1950. Trends are calculated over the 1950-2019 period.



Extended Data Fig. 6 | The complex seasonal structure of specific humidity is captured by ten harmonics. The empirical seasonal cycle of specific humidity (blue), and three different estimates of the seasonal cycle using ten seasonal harmonics (orange), a low-pass Butterworth filter with a frequency cutoff of 1/30 day⁻¹, and a 15-day moving average at two Integrated Surface Database stations. Tucson International Airport (a) is influenced by the North American monsoon, and shows a rapid change in specific humidity at its onset in July, whereas the seasonal cycle in specific humidity at Stockton Metropolitan Airport (b) does not show such rapid changes.



Extended Data Fig. 7 | The amplification index using more extreme cutoffs for hot and dry days. The ISD₁₉₇₃ amplification index used in the main text (blue) compared to a version calculated with more extreme temperature (90th-100th percentile) and specific humidity (less than 5th percentile) cutoffs (orange).